AIAA JOURNAL
Vol. 38, No. 8, August 2000

Influence of Curvature-Driven Favorable Pressure Gradient on Supersonic Turbulent Boundary Layer

Joel J. Luker*
San Antonio Air Logistics Center, Kelly Air Force Base, Texas 78241
Rodney D. W. Bowersox†
University of Alabama, Tuscaloosa, Alabama 35487
and
Thomas A. Buter‡
U.S. Air Force Test Pilot School, Edwards Air Force Base, California 93524

The influence of a wall curvature-driven favorable pressure gradient on the turbulent and mean flow properties of a Mach 2.9 boundary layer ($Re_x = 1.23 \times 10^7$) were investigated using laser Doppler velocimetry. A zero-pressure-gradient boundary layer ($Re_x = 1.35 \times 10^7$) was also mapped for comparative purposes. In addition to the typical mean and turbulent statistical properties, the data in this study were acquired with the specific goal of resolving the mean strain rates in all three coordinate directions; these data allowed for measurement of the extra Reynolds shear-stress production terms. The maximum magnitude of the distortion was 0.1, which indicated that the pressure gradient was strong. The expected stabilizing effect on the turbulence intensities was observed. Near the wall, the kinematic Reynolds shear stresses were reduced by approximately 75%. Above $y/\delta \approx 0.4$ the favorable pressure gradient induced a negative Reynolds shear stress, whereas the main strain rate remained positive. The reduced shear-stress levels were attributed to negative overall production and the use of a body-intrinsic coordinate system for data collection.

Nomenclature

d	= probe diameter or boundary-layer distortion, $e/(\partial\bar{u}/\partial y)$
e	= extra strain rate
Fl	= flatness
M	= Mach number
Re	= Reynolds number
Sk	= skewness
s	= arc length
u, v, w	= velocity components in x, y, z directions
u^*	= friction velocity, $[(\tau_w/\rho_w)^{1/2}]$
u^+	= u/u^*
γ_u	= intermittency function
$\Delta_{(\,)}$	= uncertainty in units plotted
δ_1^*	= velocity displacement thickness
δ_u	= velocity boundary-layer thickness
δ_0	= boundary-layer thickness before start of wall curvature
θ_t	= velocity momentum thickness
ρ	= density
σ	= turbulence intensity
τ_w	= wall shear stress
τ_{xy}	= incompressible Reynolds shear stress

Subscripts

e	= value at edge of boundary layer
ts	= test-section coordinate system
u, v	= measurement in u or v direction
w	= value at wall
0	= total (stagnation) value and value before wall curvature (δ_0, u_0', v_0')
1	= value in body intrinsic coordinate system
∞	= freestream value

Superscripts

T	= turbulent property
$'$	= fluctuation from Reynolds-averaged mean
$+$	= viscous length scale ($\rho_w u^*$ Length/μ_w)
$\langle\,\rangle$	= Reynolds-averaged mean

Introduction

HIGH-REYNOLDS-NUMBER supersonic flow over curved walls has many practical applications; however, detailed experimental investigations of the effects of streamline curvature-driven pressure gradients on the turbulent flow properties are scarce.[1] The lack of data has, in turn, led to a lack of understanding of the flow physics that govern supersonic turbulent boundary layers.

Although the flow physics associated with a supersonic turbulent boundary layer subjected to a pressure gradient are not fully understood, many of the salient features have been well characterized.[1–3] For example, many of the observed differences between distorted supersonic and subsonic boundary layers can be explained in terms of the fluid property changes across the boundary layer.[1,2] However, supersonic flows possess phenomena that do not have incompressible counterparts. For example, wave (expansion or compression) boundary-layer interactions, where the longitudinal pressure gradients can lead to compression or dilatation, which in turn affect the velocity, pressure, and density fluctuations, are not present in subsonic flow.

When a streamwise favorable pressure gradient is imposed on a supersonic boundary layer, the flow is distorted by both the effects of pressure gradient and by bulk dilatation. The ratio of the extra strain rates to the primary $\partial\bar{u}/\partial y$ velocity gradient,[3] called the distortion parameter, has been used as a convenient means to classify a pressure gradient. A distortion is generally considered mild if $d_{\max} \approx 0.01$ and strong for $d_{\max} \approx 0.1$ (Ref. 1). If the distortion is applied for a time that is comparable to an eddy lifetime, then the impulse parameter I, the time-integrated strain rate, may be a better choice.[2] For an impulsive perturbation resulting from a region of bulk compression, $I_p = \ell n(p2/p1)/\gamma$ (Refs. 2 and 4). For an impulse as a result of curvature, $I_\phi = \Delta\phi$ (Ref. 5). Even though the interactions between the strain rates are most likely nonlinear, the linear addition of the

Received 7 December 1998; revision received 12 July 1999; accepted for publication 29 September 1999. This material is declared a work of the U.S. Government and is not subject to copyright protection in the United States.
*Captain, U.S. Air Force. Member AIAA.
†Assistant Professor, Department of Aerospace Engineering and Mechanics. Senior Member AIAA.
‡Lieutenant Colonel, U.S. Air Force. Senior Member AIAA.

perturbation strengths is usually accepted for crude comparisons among different flows.[2]

Although few turbulence measurements have been made for the title flow, the mean flow features have been well documented.[1] For a supersonic boundary layer where the subsonic region is small compared to the boundary-layer thickness, the favorable pressure gradient causes the skin friction to decrease and the boundary-layer thickness to increase, where the opposite trend occurs for adverse pressure gradients. As discussed in Ref. 1, this counterintuitive behavior arises in supersonic flow as a result of the density decreasing more rapidly than the velocity increases through the pressure gradient region.

Collectively, the available turbulence data[6–10] indicate that the axial turbulence intensities decrease by 70–90% for I_p and I_ϕ values $\in(-0.4, -1.0)$ and $(-0.1, -0.3)$, respectively.[1,2] Because of the reduction in the fluctuating properties, as well as reductions in the skin friction and heat transfer, favorable pressure gradients are often characterized as having a stabilizing effect. Thomann[7] also demonstrated that convex curvature, with the pressure gradient removed, is also stabilizing. Relaminarization of part of the boundary layer is believed possible if the pressure gradient is strong enough.[1,8] Smith and Smits[9] and Dussauge and Gaviglio[10] estimated, using a rapid distortion analysis, that the majority of the turbulence reduction was the result of mean bulk dilatation.

Bradshaw[3] reasoned that the mean dilatational strain rate directly affects the turbulence to an extent much higher than that expected from the terms in the Reynolds-stress transport equations that contain the extra strain rates explicitly. He also proposed that when modeling supersonic pressure gradient flows with two-equation turbulence models the turbulent energy dissipation terms should be divided by a factor given by $F = 1 + \alpha d$. The constant α is on the order of 10. As noted by Bradshaw, the factor F is not a law of nature; instead it represents an empirical correction that has been successfully used to predict the effects of suddenly applied curvature, lateral divergence, and dilatation.

Of the available reports only the recent results of Arnette et al.[11] provide turbulent shear-stress data. Arnette et al. showed that the overall magnitude of the kinematic Reynolds shear stress was dramatically decreased across the entire boundary layer for 7.0 and 14.0 deg centered and gradual expansions. They further defined an apparent reverse transition, where the normal energy transfer from the mean flow had been reversed, to describe a sign changing of the Reynolds shear stress. For the gradual expansions, the study of Arnette et al.[11] provided flowfield profiles at six locations: three within the expansion and three downstream of the expansion. Although the Arnette et al. study provided detailed turbulence information throughout the expansion, the axial spacing (~2.0–4.0 cm) was not refined enough to resolve the streamwise strain rates.

The primary objective of the present study was to obtain turbulence measurements and to resolve the mean strain rates with the goal of providing insight into the physical mechanisms associated with supersonic streamline curvature-driven pressure-gradient turbulent boundary-layer flow. To meet this goal, measurements were acquired across the turbulent boundary layer over a gradual expansion ($I_p = -0.47$ and $I_\phi = -0.14$) at a single location on a measurement stencil designed specifically to resolve the mean strain rates in all three coordinate directions.

Experimental Facilities and Apparatus

Wind Tunnel and Test Section

Data were collected in a Mach 3.0 wind tunnel located at Wright–Patterson Air Force Base. The tunnel was a combination draw-down/blowdown facility. The upstream total pressure was set at a constant value of 2.13×10^5 Pa ± 1.0%. The total temperature was nominally 298 K ± 1.1%. A 27.46-cm-long (measured from the throat), finite radius, half nozzle was used to produce a freestream Mach number at the nozzle exit of 2.88 with a ±1.3% variation across the test section. The contoured side of the nozzle was located along the tunnel ceiling. The freestream turbulence intensity was nominally 0.8% at the nozzle exit. The cross-sectional shape of the test section was square, with each side being 6.35 cm in length.

The x, y, and z locations reported throughout this report are defined in body-intrinsic coordinates, with x running along the ceiling, y everywhere normal to the ceiling, z completing the right-hand system, and the origin is located at the wind-tunnel throat along the spanwise centerline. The favorable pressure-gradient model consisted of a curved ceiling for the test section. Because the main coordinate system was body-intrinsic, another coordinate system was needed to describe accurately the curvature of the wall. Thus, a test-section coordinate system was defined based on the wall geometry upstream of the start of curvature, with x_{ts} running in the streamwise direction and y_{ts} normal to the tunnel ceiling. The origin of the test-section coordinate system was located at $x = 60$ cm.

The equation for the wall curvature is given by

$$y_{ts} = \begin{cases} 0, & 0 \le x_{ts} \le 4.32 \\ -0.2078 + 0.0897x_{ts} - 9.5 \times 10^{-3}x_{ts}^2 - 3.6 \times 10^{-5}x_{ts}^3, & 4.32 \le x_{ts} \le 12.7 \\ -0.65 & 12.7 \le x_{ts} \le 16.51 \end{cases} \quad (1)$$

The units in Eq. (1) are centimeters. The wall model was forged using a computer-controlled machining device with a rated accuracy of 8 μm. The streamwise contour of the test section ceiling is provided in Fig. 1.

Data were collected at $x = 71.52$ cm (i.e., 7.20 cm downstream from the start of curvature) using both the favorable and zero-pressure-gradient models. It has been shown[12] that the tunnel boundary layer had reached a state of equilibrium at the downstream measurement station, i.e., the normalized mean flow and turbulent statistics were independent of x location (see the Boundary Layer History and Uncertainty Analysis Section for more details).

In addition to the main traverse location, measurements were taken at several additional stations to allow for strain-rate estimation. The measurement stencil was chosen to allow for second-order finite difference estimates: central differences were used in the transverse and spanwise directions, whereas upwind differences were chosen for the streamwise direction. The additional streamwise locations were located at $x = 70.98$ cm ($s/\delta_0 = 6.7$) and 70.44 cm ($s/\delta_0 = 6.2$). The spacing for this measurement stencil was nominally 0.6% of the local wall curvature. Two off-center (±0.5 cm) profiles were acquired at $x = 71.52$ cm.

Laser Doppler Velocimetry

The laser Doppler velocimetry (LDV) system was manufactured by DANTEC, Inc. The laser was an argon-ion laser with a measured

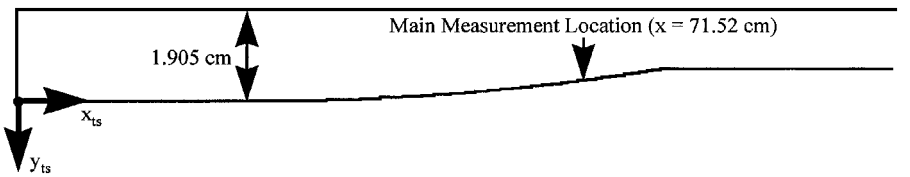

Fig. 1 Favorable pressure-gradient model and measurement location.

output capability of 275 mW. The laser was designed to operate in the TEM_{00} mode. Two wavelengths of light were used: 514.5 nm (green) and 488.0 nm (blue). A Bragg cell split each wavelength into two separate beams and supplied one of the two with a 40-MHz frequency shift. The optics were aligned in a forward scattering mode (7.0 deg off the z axis). The transmitting optics resulted in a cylindrical measurement volume that was 0.28 mm in diameter. However, the receiving optics incorporated a beam expander[12] such that a 0.14-mm-diam portion of the control volume was imaged. The data were acquired and with DANTEC 57N Enhanced Burst Spectrum Analyzers. A DANTEC three-dimensional traverse system was used to control the position of the measurement volume. The system had a rated accuracy of $\pm 80\,\mu$m over a 600-mm range (0.13 μm/mm).

The seeding apparatus consisted of a TSI, Inc., six-jet atomizer. Olive oil was chosen as the seed material and was directly injected into the tunnel stilling chamber. Based on the manufacturer's manual, roughly 90% of the particles visible to their sizing apparatus (particles with a diameter d_p less than 0.5 μm were not detected) were smaller than 1.0 μm, with a mean particle size of $d_p \approx 0.6\,\mu$m (Ref. 13). Thus, the 3-dB frequency response[14] ranged from 60 to 200 kHz, and the Stokes number ranged from 0.06 to 0.14. Finally, the expected uncertainty in the Reynolds shear stress caused by frequency response ranged from 1 to 10% but was heavily weighted toward 1% (Ref. 15).

The main traverse path ran normal to the wall at $x = 71.52$ cm ($s/\delta_0 = 7.2$). The closest position to the wall at which two-component data could be collected was $y \approx 1.13$ mm. Because the 514.5-nm beams were oriented parallel to the wall, it was possible to obtain measurements of the u-velocity component down to $y \approx 0.70$ mm.

Each data point in a given profile represents a separate tunnel run. During a given run, data were collected for a period of 12 s after the tunnel had reached steady state. Average data rates varied across the boundary layer, but were generally in the range of 0.5–2.5 kHz. To validate the data collection techniques used in this study, data were first collected in the zero-pressure-gradient test section for comparison to data in the literature[16–20]; once a positive comparison had been achieved, data collection in the favorable pressure-gradient test section was initiated. The zero-pressure-gradient comparisons are presented in the Results section.

Data-Reduction Procedures

The local Mach number was calculated from the directly measured LDV velocity and upstream total temperature in conjunction with the assumptions of adiabatic flow and a thermally and calorically perfect gas. The rms value of the fluctuating Mach number was estimated using the Strong Reynolds Analogy ($T_0' \approx 0$) and the assumption of adiabatic flow throughout the boundary layer. Miller et al.[21] showed that the total temperature turbulence intensity levels across the present boundary layers (both favorable and zero pressure gradients) were less than 3%.

Direct measurement of the intermittency was not possible with the present LDV methods. Hence, the intermittency function γ_u was obtained indirectly from the flatness data (i.e., $\gamma_u \equiv 3.0/Fl_u$) (Ref. 18). The distribution of the intermittency function was compared with the Gaussian integral curve given by $\gamma_u = 0.5(1 - erf\,\chi)$, where $\chi = (\sqrt{2}\zeta/\delta_u)^{-1}(y/\delta_u - \varphi)$. The constants ζ and φ were adjusted until the Gaussian curve matched the measured distribution; "such a curve shows that the instantaneous position of the edge of the boundary layer has random character with a mean position at $y/\delta_u = [\varphi]$."[18] The constant ζ represented the standard deviation of the boundary-layer edge from φ.

Accurate, direct measurement of the wall shear stress in the presence of a pressure gradient is very difficult.[22] Hence, an approximate indirect method was used here to estimate τ_w. Through use of the Couette flow assumption, one can see that the boundary-layer shear stress should tend toward the value of the wall shear stress. Integration of the momentum equation leads to the relation $\mu\,\partial\bar{u}/\partial y + \tau_{xy}^T = \tau_w + (\mathrm{d}p_e/\mathrm{d}x)y$. In the logarithmic region $\mu\,\partial\bar{u}/\partial y \ll \tau_{xy}^T$, and so $\tau_{xy}^T \cong \tau_w + (\mathrm{d}p_e/\mathrm{d}x)y$. Therefore, measurements of $-\overline{\rho u'v'}$ ($\approx \tau_{xy}^T$ in the Favre-averaged approach[15]) in the logarithmic region can be used along with a measurement of $\partial p_e/\partial x$ and the distance from the wall to estimate the wall shear stress. For the zero-pressure-gradient case $\partial p_e/\partial x \approx 0$, and so $\tau_{xy}^T \cong \tau_w$, and the wall shear stress can be estimated directly from the LDV measurements.

To provide confidence in the preceding technique, the wall shear stress was also calculated using the van Driest II skin-friction relationship for the zero-pressure-gradient case.[23] This relation is for turbulent flow over a flat plate. To estimate the skin friction, the zero-pressure-gradient wind tunnel was modeled as a flat plate in uniform flow where the throat of the wind tunnel was taken as the leading edge of the flat plate. However, the preexistence of a very thin boundary layer at the throat and the favorable pressure gradient generated by the expansion in the nozzle increased the uncertainty in the estimate. However, the expansion region was concentrated over the first 15% of the flow, and the Van Driest II estimate of the wall shear stress agreed to that of the Couette flow assumption to within 5.0%, which was within the $\pm 10\%$ uncertainty of the correlation.

Results and Discussion

Mean Flow Characteristics

Conventional wall-pressure measurements were acquired in the favorable pressure-gradient region at $x = 63.22$, 68.92, and 71.52 cm, and the results were $p_w/p_{0,\infty} = 0.037$, 0.025, and 0.023, respectively. Applying an upwind-difference approximation to the wall-pressure data, the streamwise derivative of the wall pressure $\partial p_w/\partial x$ was estimated as -2.0×10^4 Pa/m. The rate of change of the edge pressure $\partial p_e/\partial x$ was assumed to be equal to the rate of change of wall pressure. (Companion computational fluid dynamics results[24] support this assumption.)

All of the LDV measurements were validated by comparing the zero-pressure-gradient data collected in the current experiment to similar results from the literature. Once the credibility of the turbulence measurements was established, data were acquired in the favorable pressure-gradient boundary layer. Thus, the measurement results in this section are presented as zero-pressure-gradient data compared to the literature data. Following this, the favorable pressure-gradient data are compared to the zero-pressure-gradient data to discern the pressure gradient/curvature effects. The wind-tunnel boundary-layer properties and the uncertainty analysis are presented in the Boundary Layer History and Uncertainty Analysis Section.

For reference purposes the boundary-layer flowfield properties are summarized in Table 1. Note, for comparisons with pitot-pressure data, the Mach number boundary-layer heights were measured to be 9.0 and 11.0% larger than the velocity values listed in Table 1 for the zero and favorable pressure gradients, respectively.

The nondimensional mean u-velocity profiles for the zero and favorable pressure-gradient models are compared in Fig. 2a. Conventional probe (CP) data collected in the same facility[21] are also presented for comparison. The agreement between the present LDV and the preceding data was considered excellent. The favorable pressure-gradient boundary-layer velocity defect was slightly larger in the outer region and slightly smaller in the inner region as compared to the zero-pressure-gradient boundary layer.

The nondimensional mean v-velocity profiles are presented in Fig. 2b; data from the literature were unavailable for comparison. For the zero-pressure-gradient case v did not go to zero in the freestream as expected. This indicated a slight angular misalignment of the lasers with the wind-tunnel wall (≈ 1.7 deg). The favorable pressure

Table 1 Flowfield and boundary-layer properties

Gradient	u_e, m/s	M_e	C_f	τ_w, Pa	δ_u, mm	δ_i^*, mm	θ_i, mm	$d_{\max}$	Re/m, 1/m
Zero	602	2.8	0.0016	70.0	9.9	1.3	0.62	≈ 0	1.80×10^7
Favorable	607	2.9	0.0012	44.0	12.0	1.4	0.89	0.1	1.64×10^7

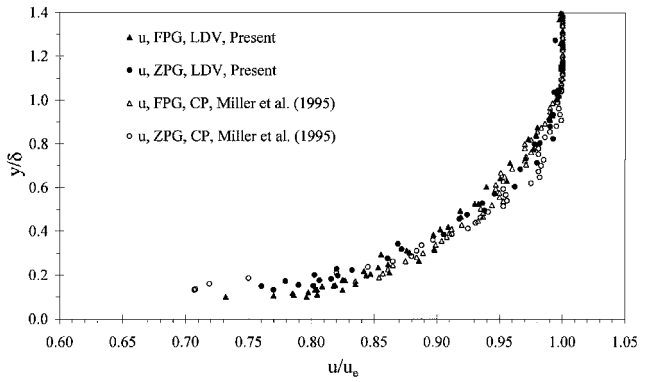

a) Streamwise mean velocity profile

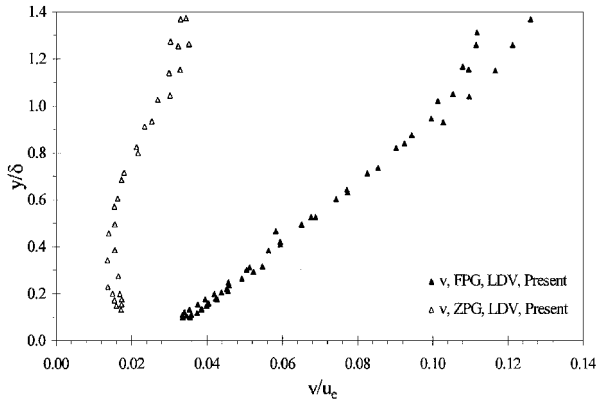

b) Normal mean velocity profile

Fig. 2 Mean velocity profiles.

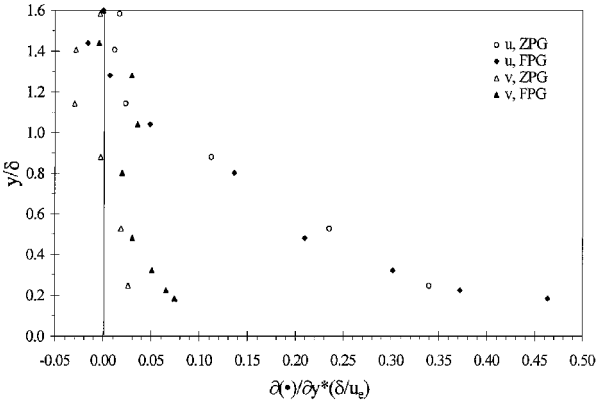

a) Wall-normal strain rates

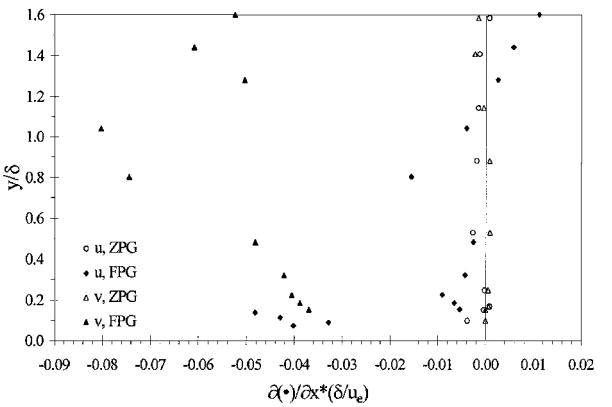

b) Streamwise strain rates

Fig. 3 Mean strain-rate profiles.

gradient had the effect of inducing a nearly linear increase in v away from the wall.

Strain-Rate Profiles

The wall-normal and streamwise strain rates are presented in Figs. 3a and 3b, respectively. The favorable pressure gradient did not have a large effect on the normalized strain rates in the direction normal to the wall (the $\partial/\partial y$ strain rates). However, the scaling factor δ/u_e was increased by 20.0% in the favorable pressure-gradient region, indicating a 20.0% increase in the absolute magnitude of the $\partial/\partial y$ strain rates as well. This increase in the absolute magnitudes also applies to the $\partial/\partial x$ strain rates.

In the outer region, the flow was accelerating ($\partial\bar{u}/\partial x > 0$). The center of the boundary layer was relatively acceleration free, and the interior boundary-layer flow was decelerating. Thus in the inner region, the flow had already accelerated as much as possible (at an upstream station) and was beginning to decelerate again. This variation in the acceleration was caused by the supersonic (i.e., hyperbolic) nature of the flow and the associated temporal/spatial interval needed to transmit wall-curvature effects downstream. Thus, as observed, the profiles of the flowfield data (mean velocities, turbulence intensities, etc.) across the boundary layer were expected to depend on the wall-curvature distribution, the distance from the wall and the Mach-number profile across the boundary layer.

The favorable pressure gradient also shifted $\partial\bar{v}/\partial x$ from the flat-plate value of zero to a finite negative value; this value decreased as y/δ increased, starting at -0.04 near the wall and decreasing to -0.08 near the freestream. This indicated greater curvature of particle trajectories near the wall (i.e., the streamlines were diverging). The values of $\partial\bar{u}/\partial z$ and $\partial\bar{v}/\partial z$ were also measured for the favorable pressure-gradient test section—these values were found to be at least an order of magnitude below any other measured strain rate and were considered negligible, as was expected for the present two-dimensional flow.

Smith and Smits[2] point out that Clauser's equilibrium parameter is not always sufficient for characterizing the strength of a pressure gradient in supersonic flows. For instance, a pressure gradient generated by a curved wall will affect the strain rates differently than the same pressure gradient generated over a flat plate or a sharp corner. Smith and Smits characterized a distortion 0.1 as strong. The maximum value of d in this study was for the $\partial\bar{v}/\partial y$ strain rate; its magnitude was approximately 0.1, which indicated that the distortion created by the favorable pressure gradient was strong.

Turbulence Intensities

Turbulence intensities were measured for both components of velocity; the zero and favorable pressure-gradient flow results are presented in Fig. 4. Normally, the turbulence intensity data are presented using Morkovin's similarity coordinates[25] in order to account for compressibility effects. However, because most of the data plotted here are at $M = 2.8$–2.9, Morkovin's scaling was not used; this minimized the uncertainty associated with the data in Fig. 4. Data from the literature are also presented for comparative purposes. Focusing first on Fig. 4a, close agreement was observed between the present u-component LDV data and that of Elena and LaCharme.[16] Although not as close, agreement with the LDV data of Robinson et al.[17] was also reasonable. In contrast, the high-speed hot-wire data of Kistler[20] and Miller et al.[21] are in close agreement with each other, but suggest significantly smaller near-wall turbulence intensities than do all of the LDV measurements. Finally, the LDV data appeared to follow the incompressible hot-wire data of Klebanoff,[18] which, based on Morkovin's hypothesis,[25] was the expected result. Similar agreement was found for the v' turbulence intensity results.

Figure 4b provides a comparison of the favorable and zero-pressure-gradient turbulence intensities. The favorable pressure gradient significantly reduced the turbulence intensities in the lower half of the boundary layer, where 70 and 30% reductions for the axial and transverse components, respectively, were seen. However, above $y/\delta \approx 0.5$ the turbulence levels were essentially unchanged. The reduction in turbulence intensities was expected given the reported

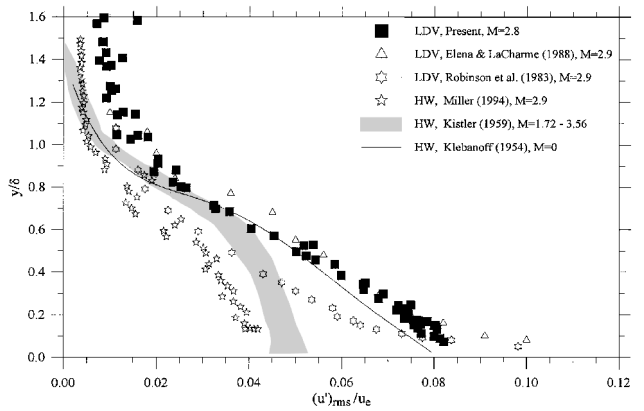

a) Zero-pressure-gradient streamwise turbulence intensities

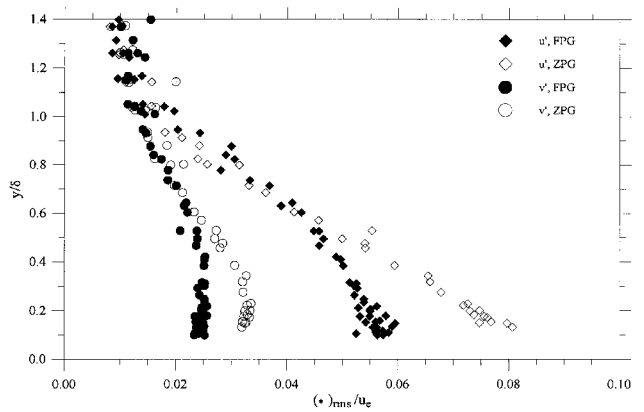

b) Favorable-pressure-gradient-to-zero-pressure-gradient comparison

Fig. 4 Turbulence intensity profiles.

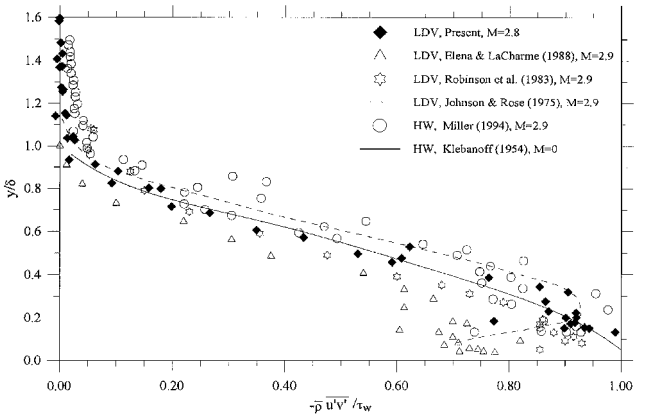

a) Zero-pressure-gradient turbulent shear stresses scaled by local wall shear stress

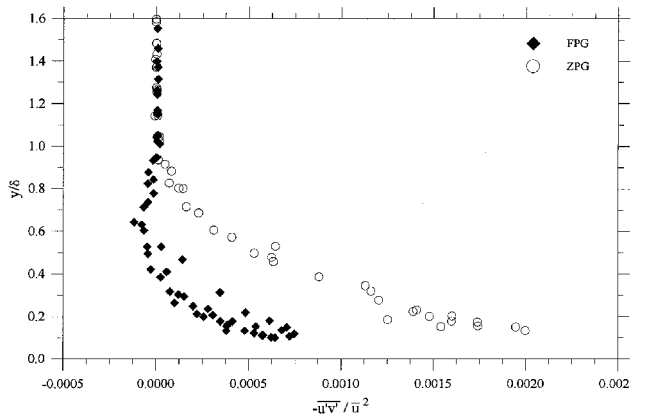

b) Favorable-pressure-gradient-to-zero-pressure-gradient comparison

Fig. 5 Turbulent shear-stress profiles.

stabilizing properties of a supersonic favorable pressure gradient.[1] In both the zero and the favorable pressure-gradient regions, the fluctuating Mach number (estimated from the data shown in Fig. 4b) was found to be much less than unity; in both cases the maximum value of M' was nominally 0.3 and was located at $y/\delta \approx 0.3$.

Reynolds Shear Stresses

Recall that the Reynolds shear stress is formally defined for compressible flows as $\tau_{xy}^T = -\bar{\rho}\overline{u'v'} - \bar{u}\overline{\rho'v'} - \bar{v}\overline{\rho'u'} - \overline{\rho'u'v'}$. Hence, within this paper the label "Reynolds shear stress" is referring to the kinematic Reynolds shear stress, i.e., $-\bar{\rho}\overline{u'v'}$. Shown in Fig. 5a is a comparison between the present zero-pressure-gradient turbulent shear-stress results and the data from previous studies; considering the relatively large scatter associated with the data and the scaling, the agreement was considered qualitatively very good. The Reynolds shear stresses scaled by local mean quantities are presented in Fig. 5b for both the favorable and zero-pressure-gradient cases. The favorable pressure gradient was seen to reduce $-\bar{\rho}\overline{u'v'}$ by approximately 75% near the wall. Based on previous studies,[1] this was the expected result. The negative Reynolds shear stresses above $y/\delta \approx 0.4$ were at first a surprising result. However, similar values were reported by Arnette et al.[11]

The negative Reynolds shear stress coupled with the positive $\partial u/\partial y$ strain rate is an intriguing feature of this flow. From a gradient transport modeling perspective, the negative shear stress translates into a negative eddy viscosity. While other researchers have measured similar negative Reynolds shear stress values,[11] the physical mechanisms, which are responsible for the change in sign, are not well understood. An examination of two mechanisms responsible for reducing the Reynolds shear stresses is presented in the next two sections.

Reynolds-Stress Production

The Reynolds-stress and strain-rate measurements allowed for the calculation of important terms in the Reynolds-stress equation. The large effects of the favorable pressure gradient on the turbulent

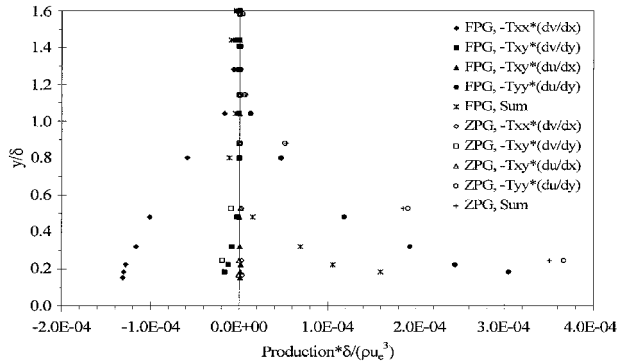

Fig. 6 Turbulent shear-stress production.

shear stresses have often been attributed to the extra production[3] (i.e., the production from terms that would normally be neglected from a boundary-layer analysis perspective). However, the magnitude of the effect is roughly an order of magnitude larger than the expected values of the extra production terms.[3] Hence, the present analysis focuses on the measurements of the Reynolds-stress production terms,[26] $-\tau_{xx}^T(\partial\bar{v}/\partial x)$, $-\tau_{xy}^T(\partial\bar{v}/\partial y)$, $-\tau_{xy}^T(\partial\bar{u}/\partial x)$, and $-\tau_{yy}^T(\partial\bar{u}/\partial y)$. The transport data were scaled by $\delta/(\bar{\rho}u_e^3)$. This scaling was used so that only directly measured LDV data are plotted in Fig. 6.

Examination of the data in Fig. 6 showed that, in the zero-pressure-gradient test section, virtually all of the Reynolds-stress production was caused by the $-\tau_{yy}^T(\partial\bar{u}/\partial y)$ term, as expected. This term also played a significant role in the favorable pressure-gradient test section as well. However, the $-\tau_{xx}^T(\partial\bar{v}/\partial x)$ term had increased as a result of the wall curvature to a point where it became significant. The negative value of $-\tau_{xx}^T(\partial\bar{v}/\partial x)$ resulted in a reduction in the magnitude of the overall sum of the Reynolds-stress production

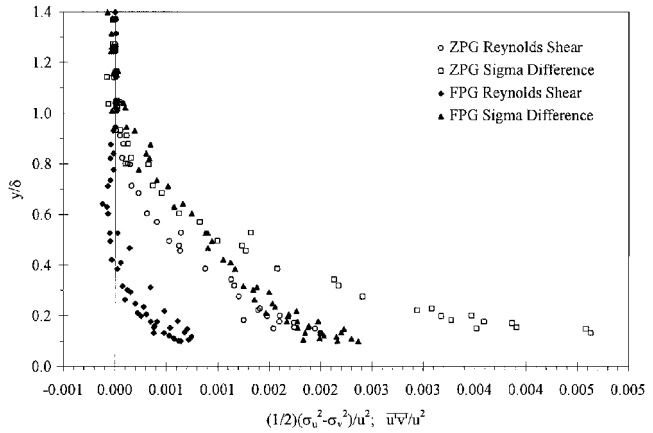

a) Comparison of terms in Eq. (2)

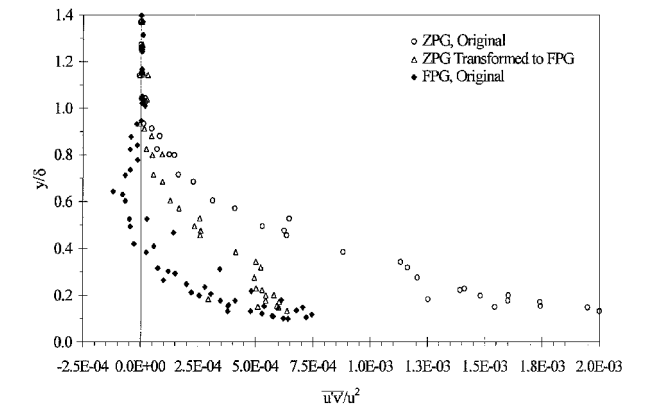

b) Transformed shear stresses

Fig. 7 Influence of the coordinate system on the turbulent shear stresses.

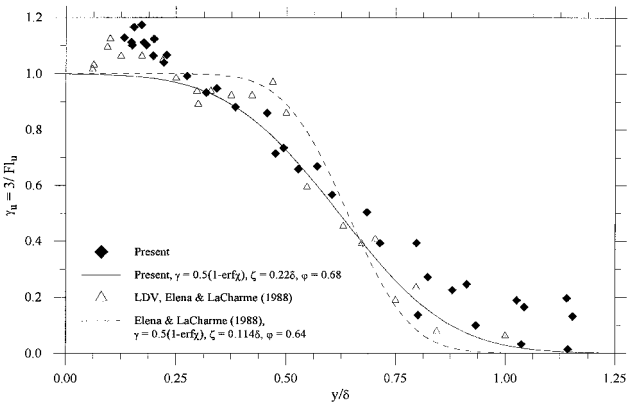

a) Zero pressure gradient

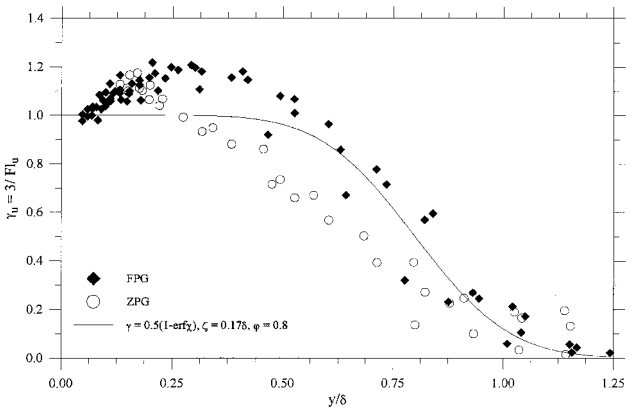

b) Favorable-pressure-gradient-to-zero-pressure-gradient comparison

Fig. 8 Intermittency profiles.

(also shown in Fig. 6). Above $y/\delta \approx 0.5$ the total Reynolds-stress production was slightly negative. The location of the negative production in the boundary-layer profile coincided with the negative Reynolds shear-stress values in Fig. 5b.

The pressure-work terms were estimated from the LDV data using the strong Reynolds analogy and the assumption of negligible pressure fluctuations. However, the magnitudes were an order of magnitude below the magnitude of the $-\tau_{xx}^T(\partial\bar{v}/\partial x)$ production term shown in Fig. 6.

Influence of the Coordinate Transformation on the Reynolds Shear Stress

The use of the body-intrinsic coordinate system also played a significant role in the shear-stress reduction. For a given transformation angle ϕ the relationship between and $\overline{u_1'v_1'}$ and $\overline{u_0'v_0'}$ is

$$\overline{u_1'v_1'} = \tfrac{1}{2}\left(\sigma_{u_0}^2 - \sigma_{v_0}^2\right)\sin(2\phi) + \overline{u_0'v_0'}\cos(2\phi) \qquad (2)$$

Figure 7a compares the term $\frac{1}{2}(\sigma_u^2 - \sigma_v^2)$ to $\overline{u'v'}$ for both the favorable pressure gradient and the zero-pressure-gradient data; in both cases the first term is at least twice the velocity correlation. The influence of the coordinate system is further demonstrated by performing the transformation of the zero-pressure-gradient data into the favorable pressure-gradient coordinate system (at the measurement location $\phi = 8.14$ deg), as shown in Fig. 7b; note that for consistency the transformed velocity correlation has been scaled by $(\bar{u}_1)^2 = (\bar{u}_0\cos\phi - \bar{v}_0\sin\phi)^2$. As the data in Fig. 7b indicate, when transforming the zero-pressure-gradient data into the favorable pressure-gradient coordinate system the magnitude of the Reynolds shear stresses were significantly reduced, but the values were still everywhere positive, indicating that the coordinate transformation alone was not responsible for the negative Reynolds shear-stress values.

The nearly equal transformed zero and favorable pressure-gradient turbulent shear-stress results in the inner region could be interpreted as indicating that the pressure gradient is not altering the Reynolds shear stresses in the near-wall region and that the entire change is caused by the coordinate transformation. Recall from the strain-rate profiles and Reynolds-stress production sections that the flow was already decelerating (implying an adverse pressure gradient, which is destabilizing[1]) in the inner region of the boundary layer, and the Reynolds-stress production in this region was positive. Thus, the near-wall shear stresses were disturbed (reduced) from their zero-pressure-gradient values by the initial acceleration and then began to increase again when the flow began to decelerate, and as shown by Smith and Smits,[9] turbulent flow properties rapidly respond to the mean flow.

Intermittency and Skewness

The flatness data were used in the calculation of the intermittency function. The profile of the zero-pressure-gradient intermittency function agreed well with the data from Elena and LaCharme[16] (Fig. 8a). The curve fit to the data from Elena and LaCharme had $\zeta = 0.114\delta$ and $\varphi = 0.64$, whereas in the present experiment the values were $\zeta = 0.22\delta$ and $\varphi = 0.68$. This showed that the boundary-layer edge was essentially at the same location as that reported by Elena and LaCharme, but the standard deviation from the mean position was almost twice as large. However, referring back to Fig. 8a, the intermittency data points between the two studies were within ~ 0.1 of each other across the boundary layer. Hence, the curve-fit parameter ζ over emphasized the differences in the two data sets.

The intermittency profile for the favorable pressure-gradient region is compared to the zero-pressure-gradient intermittency in Fig. 8b. The error function curve fit showed that for the favorable pressure-gradient region $\varphi = 0.80$ and $\zeta = 0.17\delta$. Because φ represented the random location of the boundary-layer edge, the favorable pressure gradient was seen to push this location outward as compared to the 0.68 zero-pressure-gradient result. Comparison of the magnitudes of the zero and favorable pressure-gradient intermittency profiles showed that, although the favorable pressure

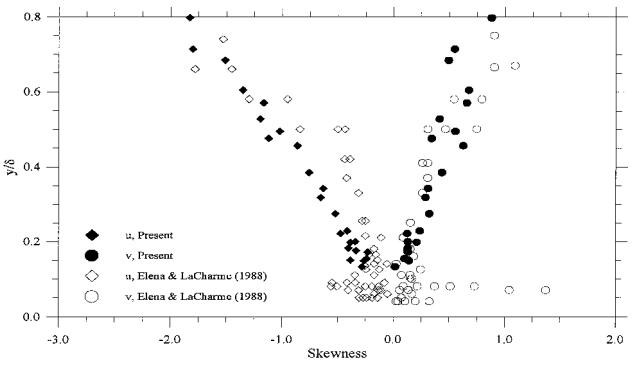

a) Zero pressure gradient

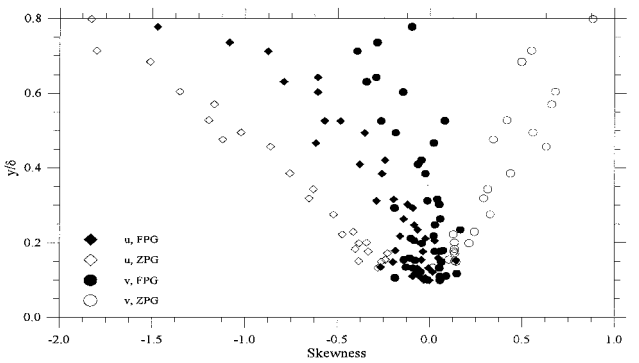

b) Favorable pressure gradient to zero pressure gradient

Fig. 9 Skewness profiles.

gradient decreased the magnitudes of the velocity fluctuations (see Fig. 4b), it caused the flow to be turbulent for a higher percentage of time. The intermittency for all of the data (including Elena and LaCharme) exceeds one. This discrepancy is attributed to the uncertainties and to the use of the flatness to provide indirect estimates of the intermittency.

Like the already described LDV data, the present zero-pressure-gradient skewness results compared very well with the results of Elena and LaCharme (Fig. 9a). Comparison of the zero and favorable pressure-gradient skewness data (Fig. 9b) showed that the favorable pressure gradient reduced the magnitude of both the u and v components of skewness. In the zero-pressure-gradient case, the high negative value of Sk_u and high positive value of Sk_v showed that more particles were crossing through the measurement volume from the side nearest the wall (below the measurement volume). The favorable pressure gradient reduced the skewness levels, indicating a more-balanced number of particles entering from above and below. In addition, in the favorable pressure-gradient case Sk_v was positive below $y/\delta \approx 0.4$ and negative farther out into the boundary layer.

Turbulent Flow Structure

The favorable pressure-gradient flow experienced an increase in the mean flow velocity and a decrease in the turbulence intensities. When taken together, these two pieces of data indicated that the slower particles were getting accelerated more than the faster-moving particles. The additional acceleration given to the slower particles can be explained using basic physical arguments: as the particles traveled through the pressure-gradient region, they received an impulse $I = \int F\,dt$, where F is the force applied to a particle over time. The force applied by the pressure gradient is a function of position only $[F = F(x, y)]$ so that $I = \int (F/V)\,ds$, where V represents the magnitude of the particle's total velocity and ds is the distance traveled by the particle. Thus, for a given trajectory through the pressure-gradient region, the slower-moving particles received a larger impulse and were accelerated more than the faster-moving particles. If the pressure-gradient region is strong and long enough, eventually all of the particles would travel at the same speed, i.e., the flow would be relaminarized.

On the average the particles nearer to the wall were traveling slower than those farther out in the freestream and were also subjected to a larger force per unit length than the freestream particles. Thus, the mean velocity in the inner portion of the boundary layer was increased more than the mean velocity in the outer region. This would appear as a smaller velocity defect in the inner portion of the favorable pressure-gradient boundary layer. Although this reduced velocity defect was not readily apparent in Fig. 2b, it was obvious in the data presented by Arnette.[11] The reason this difference in the velocity profile is not apparent in the present study is a result of the strain-rate variation across the boundary layer, specifically the deceleration in the inner region of the boundary layer.

The favorable pressure gradient increased the intermittency. For the intermittency to increase while the turbulence intensities decreased, the large-scale eddies must have been broken down into a greater number of smaller-scale eddies. That is, the intermittency was increased because of a larger number of eddies, but each eddy had a smaller fluctuating velocity. The reduced fluctuation levels and reduced shear-stress correlation coefficients (turbulent shear stress normalized by the axial and transverse turbulence intensities) are used as indicators that the flow is becoming more isotropic. It is not suggested here that the flow was becoming isotropic, instead the tendency of the flow to approach an isotropic state is taken to enhance the notion that the large-scale structures were disintegrating. The tendency of the flow to approach isotropy is also consistent with the skewness measurements, where the skewness measurements indicated that the favorable pressure gradient evened out the number of particles entering the measurement volume. The breakdown of the turbulent structures is also consistent with the overall stabilizing effect of the favorable pressure gradient, where, as energy is redistributed to the smaller turbulent scales, the amount of available energy to be dissipated by the flow increases[27] and the flow becomes more stable.

Boundary-Layer History and Uncertainty Analysis

The wind-tunnel boundary-layer history and a detailed uncertainty analysis are described in this section. Shown in Fig. 10a are the mean velocity and turbulent shear-stress profiles obtained at $x = 44.0$, 71.52, and 81.46 cm. As indicated, the mean and turbulent statistical flow properties had achieved equilibrium by the $x = 44.0$ cm location (i.e., when plotted as scaled in Fig. 10, the data collapse). The skin-friction coefficients and boundary-layer heights, along the tunnel centerline, are plotted in Fig. 10b. The skin-friction coefficient was directly measured with a floating element skin-friction sensor[28] at $x = 81.46$ cm, and the result agreed to within 2.0% of the Van Driest II prediction, as shown. The Couette flow assumption produced results that agreed to within 5.0% of the Van Driest II correlation at $x = 71.52$ cm. Applying the Couette flow assumption to the Miller et al.[21] cross-film data in Fig. 10, the skin-friction coefficient at $x = 44.0$ cm was estimated as 0.00185 with a relatively large scatter of approximately ±15%. The Van Driest II skin-friction coefficient at this location was 0.00172, which was within 7.0% of the Couette flow estimate. The boundary-layer height correlation that resulted from integrating the integral momentum equation, assuming a flat plate starting at the nozzle throat and $\frac{1}{7}$th velocity power law[29] and correcting for compressibility as described in Van Driest,[23] produced the correlation shown in Fig. 10b that agreed with the measurements to within ±5.0%.

A standard uncertainty analysis,[30] accounting for proble location, transducer calibration, and repeatability (95% confidence interval, assuming a Student t distribution over 18–20 tests[30]), was performed for the conventional pressure and temperature probe data. The uncertainties in the freestream total pressure, static pressure, total temperature, and Mach number were estimated as ±1.0, ±6.4, ±1.1, and ±1.5%, respectively.

The uncertainty analysis of the LDV data accounted for probe volume location, record length, velocity gradient broadening,[31,32] laser-beam angular alignment, seed bias,[32] density bias, coincidence filtering, and repeatability. The results of the uncertainty analysis are summarized in Table 2, and the procedures are outlined next.

The probe volume location analysis follows the procedures outlined in Ref. 30. The probe position uncertainty was 0.074 mm

Table 2 Uncertainty estimates[a] (in the units plotted in Figs. 2–9)

y/δ	$\Delta_{\bar{u}/u_e}$ (×10²)	$\Delta_{\bar{v}/u_e}$ (×10²)	$\Delta_{\sqrt{\overline{u'^2}}/\bar{u}_e}$ (×10³)	$\Delta_{\sqrt{\overline{v'^2}}/\bar{u}}$ (×10³)	$\Delta_{\overline{u'v'}/\bar{u}^2}$ (×10⁴)	Δ_{Sku} (×10)	Δ_{Skv} (×10)	Δ_{γ} (×10)
0.07[b]	2.1, 1.6	2.6, 2.6	2.6, 1.7	NA	NA	5.1, 5.6	NA	1.9, 1.8
0.15	1.3, 1.1	2.8, 2.8	2.1, 1.3	0.8, 0.7	0.2, 0.2	2.7, 2.7	1.0, 1.0	1.9, 1.7
0.20	1.3, 1.1	2.8, 2.8	2.1, 1.3	0.8, 0.7	0.7, 0.1	2.3, 2.2	1.2, 1.0	1.9, 1.8
0.30	1.5, 1.2	3.0, 3.0	2.1, 1.3	0.8, 0.7	1.0, 0.3	2.6, 1.9	2.0, 1.3	1.7, 1.9
0.50	1.4, 1.2	3.3, 3.3	1.9, 1.3	1.1, 0.8	2.9, 0.4	3.8, 2.2	4.4, 3.0	1.4, 1.9
1.00	1.2, 1.2	3.5, 3.5	1.5, 0.9	1.1, 0.7	0.4, 0.2	5.8, 3.8	4.8, 8.3	0.4, 0.6

y/δ	$\Delta_{d\bar{u}/dy}$ (×10)	$\Delta_{d\bar{u}/dx}$ (×10²)	$\Delta_{d\bar{v}/dy}$ (×10³)	$\Delta_{d\bar{v}/dx}$ (×10⁴)	$\Delta_{\tau_{xx}dv/dx}$ (×10⁵)	$\Delta_{\tau_{xy}dv/dy}$ (×10⁶)	$\Delta_{\tau_{xy}du/dx}$ (×10⁵)	$\Delta_{\tau_{yy}du/dy}$ (×10⁴)
0.15	1.5, 1.1	2.0, 1.5	1.4, 4.5	2.7, 8.3	1.7, 3.1	1.4, 2.1	2.0, 0.7	1.5, 0.7
0.20	0.9, 0.8	1.3, 1.1	3.0, 5.4	5.6, 10	3.5, 3.9	3.2, 0.8	1.4, 0.1	1.0, 0.6
0.30	0.9, 0.8	1.4, 1.2	3.6, 6.9	6.6, 13	4.5, 5.6	1.9, 0.5	0.8, 0.0	1.0, 0.7
0.50	1.0, 0.9	1.6, 1.4	3.1, 9.1	5.8, 17	3.8, 8.0	1.4, 1.3	0.7, 0.1	0.8, 0.7
1.00	1.0, 0.9	1.7, 1.5	4.3, 13	7.0, 17	4.7, 10	0.1, 2.4	0.0, 0.1	0.2, 0.2

[a]Left entry: zero pressure gradient; right entry: favorable pressure gradient.
[b]Single-component x data were acquired for $y/\delta < 0.15$.

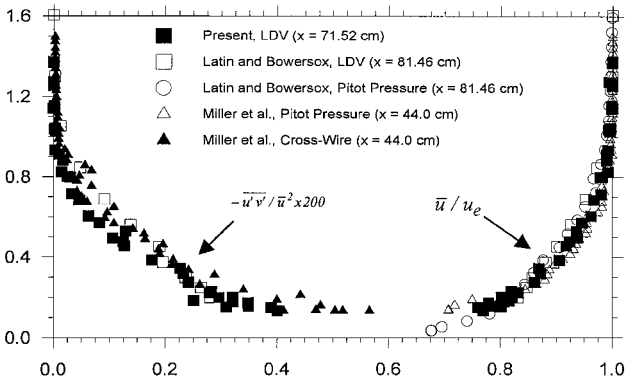

a) Turbulent shear-stress and mean velocity profile data

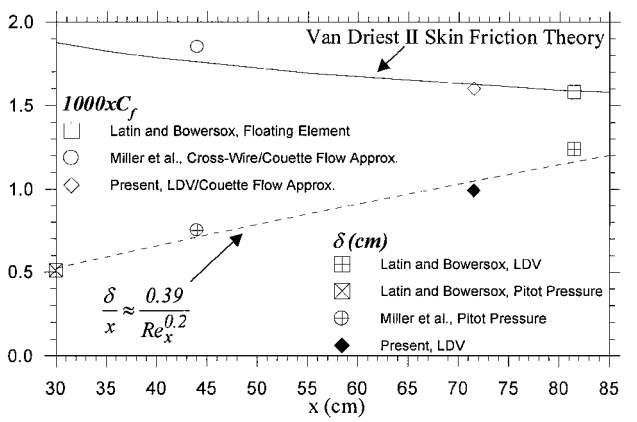

b) Skin-friction and boundary-layer thickness

Fig. 10 Zero-pressure-gradient flowfield properties along the tunnel centerline.

plus an accumulation that resulted from a 0.01-mm hysteresis. For the present record length of 16, the record length uncertainties in u and v were ±0.095 and 0.090 m/s (based on manufacturer's specifications), respectively. Gradient broadening bias results from the velocity gradient across the measurement volume. The error in the mean velocity is caused by the nonlinearity of the velocity profile across the measurement volume. A conservative estimate was derived, assuming the logarithmic profile across the boundary layer. Because the v/u_e was nearly constant or linear for the zero pressure gradient and favorable pressure-gradient flows, respectively, $\Delta_{\bar{v}/u_e} \cong 0$. The relations for statistical properties relations (the remaining columns in Table 2) were obtained by assuming that the velocity within the control volume could be represented by a Taylor series, where only the first-order term was retained.[31] The u-velocity gradient was estimated by differentiating the theoretical law of the wall equation with the wake function included.[29] The v-velocity gradient was zero for the zero pressure gradient and ~4000/s (see Fig. 2b) for the favorable pressure gradient. The angular alignment uncertainty relations were estimated by applying an angular rotation with small angle approximations, where $\Delta\phi$ was approximately ±0.035 rad. Seed bias results because the probe volume experiences a larger number of higher velocity particles.[32] The proper method of averaging to account for seed bias remains unproven; however, the suggestion was made that the statistical averages should be weighted by the particle transit time.[32] The seed bias uncertainty was derived by defining the uncertainty by the difference between conventional time averaging (the method used here) and the particle-transit-time-weighted average. Similarly, density bias results because the higher densities contain a larger concentration of particles. Hence, the burst spectrum analyzer registers a larger number of the higher-density flow particles. As was the case for the seed bias, the density bias relations were derived by defining the difference between conventional time averaging and a density-weighted averaging as the uncertainty. To simplify the analysis, the strong Reynolds analogy[1] was invoked. The resulting seed and density bias equations were similar in form and were combined, taking into account that the higher velocity flow had a lower density. Coincidence filtering was performed to ensure that both the u- and v-component burst spectrum analyzers were observing the same particle. The coincidence filtering uncertainties were estimated by processing the data with and without coincidence filtering and taking the difference between two outputs. A 95% confidence interval (assuming a Student t distribution with 18 samples) was used to quantify the data repeatability. Propagation of the preceding uncertainties through all of the acquired data was performed.[30] The total uncertainty values listed in Table 2 (in the units plotted in Figs. 2–9) were obtained by an Euclidean norm of the uncertainties just listed.[30] Because the uncertainties were small, corrections were not applied.

Conclusions

The main goal of the present study was to use LDV to investigate the effects of a favorable pressure gradient on the mean and turbulent flow properties of a supersonic boundary layer ($M = 2.9$, $Re_x = 1.23 \times 10^7$). A specific goal of the present work was the resolution of the mean strain rates to aid in interpreting the experimental results. A detailed examination of the flow properties and processes was performed to provide insight into the physics involved with supersonic curvature-driven favorable pressure-gradient flow. In general, the results of this study describe the influence of the wall curvature-driven favorable pressure gradient on the mean and turbulent statistical flow properties.

Overall, the turbulence data indicated that the present favorable pressure gradient had the expected stabilizing effect on the turbulent quantities. Near the wall the streamwise turbulence intensities were about 30% of the corresponding zero-pressure-gradient value, but above a height of $y/\delta \approx 0.5$ the favorable pressure gradient had

relatively little effect. The magnitude of the Reynolds shear stress was also reduced by the favorable pressure gradient; in the near-wall region it was approximately 25% of the zero-pressure-gradient value, and in the outer region ($y/\delta > 0.5$) the kinematic Reynolds shear stresses were negative and the principle strain rates positive. The three-dimensional strain-rate measurements and the associated extra production indicated that the overall turbulence production was also negative in the outer half of the favorable pressure-gradient boundary layer. In addition, the use of a body-intrinsic coordinate system contributed to the reduced shear-stress levels. A result that had an important impact on the local flow structure, which was determined from the strain-rate measurements, was that the favorable pressure-gradient axial velocity was accelerating in the outer half of the boundary layer and decelerating in the lower half. This variation in the axial strain rates influenced the turbulence levels across the boundary layer. Last, the present data collectively indicated that the favorable pressure gradient was disintegrating the large-scale eddies into smaller ones. This redistribution of energy increased the amount of turbulent energy available for dissipation by the flow, which in turn had the observed stabilizing effect on the boundary layer.

Acknowledgment

The authors would like to gratefully acknowledge Jim McMichael of the Air Force Office of Scientific Research for sponsoring this work.

References

[1]Spina, E. F., Smits, A. J., and Robinson, S. K., "The Physics of Supersonic Turbulent Boundary Layers," *Annual Review of Fluid Mechanics*, Vol. 26, 1994, pp. 287–319.

[2]Smith, D. R., and Smits, A. J., "The Effects of Streamline Curvature and Pressure Gradient on the Behavior of Turbulent Boundary Layers in Supersonic Flow," AIAA Paper 94-2227, June 1994.

[3]Bradshaw, P., "The Effect of Mean Compression or Dilatation on the Turbulence Structure of Supersonic Boundary Layers," *Journal of Fluid Mechanics*, Vol. 63, No. 3, 1974, pp. 449–464.

[4]Hayakawa, K., Smits, A., and Bogdonoff, S., "Hot-Wire Investigation of an Unseparated Shock/Boundary Layer Interaction," *AIAA Journal*, Vol. 22, No. 4, 1984, pp. 579–585.

[5]Smits, A., Young, S., and Bradshaw, P., "The Effects of Short Regions of High Surface Curvature on Turbulent Boundary Layers," *Journal of Fluid Mechanics*, Vol. 94, Sept. 1979, pp. 209–242.

[6]Donovan, J., Spina, E., and Smits, A., "The Structure of Supersonic Turbulent Boundary Layers Subjected to Concave Surface Curvature," *Journal of Fluid Mechanics*, Vol. 259, Jan. 1993, pp. 1–24.

[7]Thomann, H., "The Effects of Streamwise Wall Curvature on Heat Transfer in Turbulent Boundary Layers," *Journal of Fluid Mechanics*, Vol. 33, July 1968, pp. 283–292.

[8]Jayaram, M., Taylor, M., and Smits, A., "The Response of a Compressible Turbulent Boundary Layer to Short Regions of Concave Surface Curvature," *Journal of Fluid Mechanics*, Vol. 175, Feb. 1987, pp. 343–362.

[9]Smith, D., and Smits, A., "The Rapid Expansion of a Turbulent Boundary Layer in a Supersonic Flow," *Theoretical Computational Fluid Dynamics*, Vol. 2, 1991, pp. 319–328.

[10]Dussuage, J., and Gaviglio, J., "The Rapid Expansion of a Supersonic Flow: The Role of Bulk Dilatation," *Journal of Fluid Mechanics*, Vol. 174, Jan. 1987, pp. 81–112.

[11]Arnette, S. A., Samimy, M., and Elliott, G. S., "The Effects of Expansion Regions on the Turbulence Structure of Compressible Boundary Layers," AIAA Paper 96-0656, Jan. 1996.

[12]Luker, J. J., "Laser-Doppler Velocimetry Measurements in a Supersonic Boundary Layer Including Favorable Pressure Gradient Effects," M. S. Thesis, Dept. of Aeronautics and Astronautics, Air Force Inst. of Technology, AFIT/GAE/ENY/95D-15, Wright–Patterson AFB, OH, Dec. 1995.

[13]TSI, Inc., "Model 9306 Six-Jet Atomizer Instruction Manual," 1990143 Rev. F, St. Paul, MN, May 1996.

[14]Menon, R., and Lai, W., "Key Characteristics in the Selection of Seed Particles for LDV Measurements," *Proceedings of the Fourth International Conference on Laser Anemometry, Advances and Applications*, edited by A. Dybbs and B. Ghorashi, American Society of Mechanical Engineers and European Association For Laser Anemometry, Cleveland, OH, 1991, pp. 719–730.

[15]Bowersox, R. D. W., "Combined Laser Doppler Velocimetry and Cross-Wire Anemometry Analysis for Supersonic Turbulent Flows," *AIAA Journal*, Vol. 34, No. 11, 1996, pp. 2269–2275.

[16]Elena, M., and LaCharme, J.-P., "Experimental Study of a Supersonic Turbulent Boundary Layer Using a Laser Doppler Anemometer," *Journal of Theoretical and Applied Mechanics*, Vol. 7, No. 2, 1988, pp. 175–190.

[17]Robinson, S. K., Seegmiller, H. L., and Kussoy, M. I., "Hot-Wire and Laser Doppler Anemometer Measurements in a Supersonic Boundary Layer," AIAA Paper 83-1723, July 1983.

[18]Klebanoff, P. S., "Characteristics of Turbulence in a Boundary Layer with Zero Pressure Gradient," National Committee for Aeronautics, Rept. 1247, National Bureau of Standards, May 1954; also NASA TN 3178, May 1954.

[19]Johnson, D. A., and Rose, W. C., "Laser Velocimeter and Hot-Wire Anemometer Comparison in a Supersonic Boundary Layer," *AIAA Journal*, Vol. 13, No. 4, 1975, pp. 512–515.

[20]Kistler, A., "Fluctuation Measurements in a Supersonic Turbulent Boundary Layer," *Physics of Fluids*, Vol. 2, No. 3, 1959, pp. 290–296.

[21]Miller, R., Dotter, J., Bowersox, R. D. W., and Buter, T. A., "Compressible Turbulence Measurements in Supersonic Boundary Layers with Favorable and Adverse Pressure Gradients," *Transitional and Turbulent Compressible Flows*, edited by L. Kral, E. Spina, and C. Arakawa, FED-Vol. 224, American Society of Mechanical Engineers, New York, 1995, pp. 193–200.

[22]Hazelton, D., Bowersox, R., and Schetz, J., "Directional Skin Friction Measurements in a High Enthalpy Supersonic Flow About a Sharp Fin," AIAA Paper 96-4503, July 1996.

[23]Van Driest, E. R., "Turbulent Boundary Layers in Compressible Fluids," *Journal of the Aeronautical Sciences*, Vol. 18, No. 3, 1951, pp. 145–160.

[24]Fick, E., Gaitonde, D., and Buter, T., "Numerical Simulation of Supersonic Turbulent Boundary Layer Flow with Mild Pressure Gradients," AIAA Paper 96-2059, July 1996.

[25]Morkovin, M. V., "Effects of Compressibility on Turbulent Flows," *The Mechanics of Turbulence*, Gordon and Breach, New York, 1964, pp. 367–380.

[26]Wilcox, D., *Turbulence Modeling for CFD*, DCW Industries, Inc., Glendale, CA, 1993.

[27]Hinze, J. O., *Turbulence*, 2nd ed., McGraw–Hill, New York, 1975.

[28]Latin, R., and Bowersox, R., "Influence of Surface Roughness on the Mean and Turbulent Flow Properties of Supersonic Boundary Layer," AIAA Paper 99-1017, Jan. 1999.

[29]Schetz, J., *Boundary Layer Analysis*, Prentice–Hall, Upper Saddle River, NJ, 1993.

[30]Holman, J. P., *Experimental Methods for Engineers*, 3rd ed., McGraw–Hill, New York, 1978, pp. 41–82.

[31]Durst, F., Melling, A., and Whitelaw, J., *Principles and Practice of Laser-Doppler Anemometry*, Academic, New York, 1981, pp. 203–212.

[32]Adrian, R., "Laser Velocimetry," *Fluid Mechanics Measurements*, 2nd ed., edited by R. Goldstein, Taylor and Francis, Washington, DC, 1996, pp. 175–293.

M. Samimy
Associate Editor